Eur. Phys. J. E (2015) **38**: 27
DOI 10.1140/epje/i2015-15027-2

THE EUROPEAN PHYSICAL JOURNAL E

Regular Article

Contribution to the benchmark for ternary mixtures: Measurement of the Soret, diffusion and thermodiffusion coefficients in the ternary mixture THN/IBB/nC$_{12}$ with 0.8/0.1/0.1 mass fractions in ground and orbital laboratories*

A. Mialdun[a], J.-C. Legros, V. Yasnou, V. Sechenyh, and V. Shevtsova

MRC, Université Libre de Bruxelles (ULB), av. F. Roosevelt, 50, Brussels, Belgium

Received 21 July 2014 and Received in final form 5 November 2014
Published online: 27 April 2015 –

Abstract. We have determined the Soret (S_T), diffusion (D), and thermodiffusion (D_T) coefficients in a ternary mixture of tetralin–isobutylbenzene–*n*-dodecane with a composition of 0.80/0.10/0.10 by mass fraction at a temperature of 298 K. The Soret coefficients were measured in the microgravity experiment DCMIX1 and on the ground by optical digital interferometry (ODI) using two lasers with different wavelengths. The values of the Soret coefficients were determined from the stationary separation of the components using two- and six-parameter fits. The diffusion coefficients were independently measured using the Taylor Dispersion Technique in the ground laboratory, and the thermodiffusion coefficients were derived from known S_T and matrix D. The processing of the data from the DCMIX experiment conducted on the International Space Station is discussed in detail. The multi-user design of the on-board instrument causes perturbations in the component separation. Several recommendations are suggested for improving the quality of the microgravity results. For example, we demonstrated that the tomography reconstruction of the 3-D concentration field allows to restore the underestimated component separation resulting from the spatial non-linearity of the temperature field. Furthermore, to avoid errors in component separation due to mass exchange between the working liquid volume and the expansion volume at the top of the cell, we suggest considering the evolution of the separation only in the lower half of the cell. The results of this study displayed reasonable quantitative agreement between the microgravity and ground experiments.

1 Introduction

The DCMIX (Diffusion Coefficients in Mixtures) project consists of a series of microgravity experiments designed to study thermodiffusion (also known as thermal diffusion or the Soret effect) in different ternary liquid systems. This project involves a large international group of scientists.

In ternary mixtures, when pressure diffusion is negligible, the diffusive fluxes of two independent components are driven by concentration and temperature gradients:

$$J_1 = -\rho(D_{11}\nabla C_1 + D_{12}\nabla C_2) - \rho D'_{T,1}\nabla T, \quad (1)$$

$$J_2 = -\rho(D_{21}\nabla C_1 + D_{22}\nabla C_2) - \rho D'_{T,2}\nabla T. \quad (2)$$

Here, C_1, C_2 are the corresponding mass fractions, D_{ij} are the mass-based diffusion coefficients, and $D_{T,i}$ are the thermodiffusion coefficients, which can be written as $D'_{T,i} = C_i(1-C_i)D_{T,i}$. In the steady state, the mass fluxes vanish, $J_i = 0$, and eqs. (1)–(2) can be written as

$$\nabla C_i^{\mathrm{st}} = -S'_{T,i}\nabla T, \quad (3)$$

where the Soret coefficients $S'_{T,i}$ are defined as

$$S'_{T,1} = \frac{D'_{T,1}D_{22} - D'_{T,2}D_{12}}{D_{11}D_{22} - D_{12}D_{21}},$$

$$S'_{T,2} = \frac{D'_{T,2}D_{11} - D'_{T,1}D_{21}}{D_{11}D_{22} - D_{12}D_{21}}.$$

The primary objective of experimental efforts is to determine four mass diffusion and two thermodiffusion coefficients. Although experimentally difficult and challenging, the measurement of thermodiffusion in ternary mixtures has attracted the attention of researchers and has developed very rapidly [1–5]. However, even in well-established techniques, the buoyancy-driven convection may appear in ternary mixtures because the signs of the Soret coefficients of the various components could be different, and it destabilizes the system [6]. In this respect,

* Contribution to the Topical Issue "Thermal non-equilibrium phenomena in multi-component fluids" edited by Fabrizio Croccolo and Henri Bataller.

[a] e-mail: amialdun@ulb.ac.be

the microgravity platform offers the invaluable advantage of convection-free conditions. This platform allows for both the benchmarking of ground measurements and performing unique experiments that are currently only possible in orbit.

The microgravity set-up uses optical digital interferometry (ODI) to measure concentration separation caused by the Soret effect. The extraction of data from an experiment with interferometric probing is a non-trivial task in itself. In the particular case of DCMIX, this task is complicated by the use of a non-standard cell design [7], which makes processing of the experimental data even more complex. This complexity requires the use of some assumptions and simplifications, which can lead to differences in the results obtained from the same raw data by different research groups. To form a solid background for correct data processing, several groups agreed to process similar datasets from the microgravity experiment and to compare the results. The DCMIX1 experiments consisted of 5 ternary compositions of the mixture THN (tetralin)–IBB (isobutylbenzene)–nC$_{12}$ (n-dodecane). The selection of one of these compositions as the benchmark was made during the meeting of the topical team "Diffusion in non-metallic liquids" of the European Space Agency held in October 2013 in Mondragon, Spain. The ternary mixture THN/IBB/nC$_{12}$ with mass fractions 0.80/0.10/0.10 was selected as the benchmark.

The overall purpose of the benchmark was two-fold. The second, equally important objective was to benchmark this mixture with all available ground measurement techniques.

This paper is a contribution to the benchmark by the group from Université Libre de Bruxelles (led by V. Shevtsova), and it includes benchmarking contributions for the processing of both microgravity experiments and ground measurements.

2 Experimental

2.1 On-board instrument SODI

The Selectable Optical Diagnostics Instrument (SODI) was designed to measure Soret coefficients on board the International Space Station (ISS). A detailed description of the instrument was given in [7], and thus, we will only briefly outline the main features here.

The SODI is based on the optical digital interferometry technique and uses a two-wavelength Mach-Zehnder interferometer in which laser diodes with wavelengths of 670 and 935 nm serve as sources of coherent illumination. Henceforth, we will refer to these laser diodes as red and infrared lasers, respectively. Furthermore, the refractive indices measured at these wavelengths will be subscripted as (1) for the red laser and as (2) for the infrared laser. Interferograms formed by both beams are recorded almost simultaneously during the experiment.

The interferometer is aligned for the wide fringe configuration because the phase-shift technique was proposed for optical phase extraction from raw fringes [8].

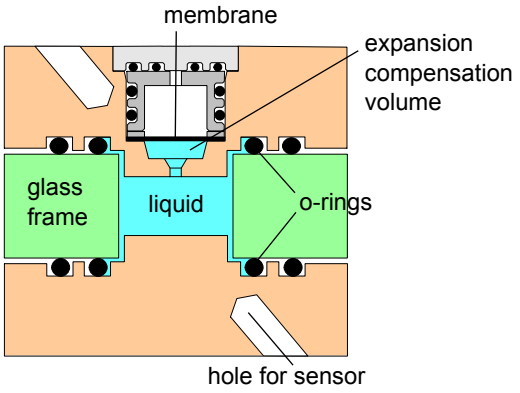

Fig. 1. Schematic of the central part of the experiment cell.

A transparent rectangular cell with inner dimensions of 10 mm × 10 mm × 5 mm is filled with a liquid mixture. The glass frame is clamped from the top and bottom between two copper blocks thermally stabilized by Peltier elements, which maintain a temperature gradient across the cell. The diffusion path (*i.e.*, the distance between the working surfaces of the plates) is $H = 5.0$ mm. Five cells with ternary mixtures of different concentrations (primary cells) and one cell with the reference binary mixture (companion cell) are integrated into a one-piece structure, which is called the cell array.

The SODI is a multi-user instrument, and the test cell has specific features in the design (see fig. 1). To facilitate observation of the full liquid volume, the copper blocks have protrusions that enter the opening in the glass frame by approximately 2 mm. Furthermore, due to the double-containment requirement (*i.e.*, leakage-preventing barrier), there are two rubber O-rings between the glass frame and each copper block. The blocks, in turn, contain grooves to accommodate these seals. This cell geometry leads to a strong deviation of the temperature field from linearity in the vertical direction, particularly in the corners of the cell. This deviation was also observed during the IVIDIL experiment [9].

Another feature of the cell design that affects the thermodiffusion separation process is the presence of a compensation volume for thermal expansion. This forms a *dead* volume with a nearly isothermal liquid, which is not directly involved in the Soret separation, but it indirectly perturbs the separation through diffusive mass exchange with neighboring regions already affected by thermodiffusion. Other *dead* volumes are formed by 0.5 mm thick grooves between the glass walls and protrusions of the copper blocks.

The importance of considering the influence of the dead volumes was first recognized in [7], and hereafter, it will be discussed in more detail as one of the key points for data evaluation.

Our study is focused on the mixture THN/IBB/nC$_{12}$ with mass fractions of 0.80/0.10/0.10 in the selected cell #3. Hereafter, the following numbering of the components is used: (1) tetralin (THN) – (2) isobutylbenzene (IBB) – (3) n-dodecane (nC$_{12}$). These numbers will be used as

subscripts when designating the concentration of the corresponding component C_i. Data evaluation was performed for one of the experimental runs carried out with this cell, namely, Run #18, which started 02-Dec-2011 21:43 and ended 03-Dec-2011 08:06 UTC. Experiments in this cell were repeated several times, but we will only present the results for one run. Our experience with the IVIDIL experiment on board the ISS inside the SODI instrument showed [9–11] that the microgravity results are well reproduced.

2.2 Ground ODI set-up

The optical digital interferometry technique (ODI) was used to determine the Soret coefficients on the ground. The only change with respect to the set-up described in detail in [12] is the slightly modified design of the Soret cell. To overcome the problem of solvent permeating through the rubber O-rings, the seals were replaced with ones composed of indium. We have confirmed that the new design has no issue with lateral heat fluxes in the experimental cell. Unlike the microgravity cell, the copper blocks in the ground cell are flat and do not contain protrusions, and the height of the cell is $H = 6.06\,\text{mm}$.

Two laser diodes with wavelengths of 670 and 925 nm were chosen to be as close as possible to the wavelengths utilized by the SODI. Only one laser is used in each experiment, and then, it is replaced by the other laser. The light source units have identical designs with standardized electrical connectors and mechanical fixations, which allows the lasers to be exchanged without touching the optical elements or the cell. Thus, replacing the light source did not affect either the alignment of the interferometer and recording system or the cell. The thermodiffusion experiments in the ground laboratory were repeated three times with each laser. The test liquid mixture was the same during all the experimental runs, which lasted approximately two weeks.

Each time before switching the temperature difference on, the full set-up, including the interferometer and cell, was maintained at the mean temperature for 24 hours. In all cases, the duration of the Soret separation phase was 16 hours.

2.3 Taylor dispersion set-up

Isothermal diffusion coefficients were measured using the recently developed and tested Taylor dispersion instrument outlined in [13]. To characterize ternary diffusion in the mixture of interest, we performed 3 different injections (with distinct concentration differences from the base solution) and repeated each injection 3-4 times, thus providing 11 runs for simultaneous processing.

The chemicals used to prepare the mixture were 1,2,3, 4-tetrahydronaphthalene (Acros Organics, 98+%), isobutylbenzene (Acros Organics, 99.5%), and *n*-dodecane (Acros Organics, 99%). The chemicals were used without further purification, but the prepared mixture was continuously degassed during the course of the experiment.

3 Data evaluation

In this section, we discuss the main features and difficulties regarding the processing of data from the microgravity and ground-based experiments. The results from applying this procedure will be presented in the next section.

3.1 Analysis of data obtained in the microgravity experiment

One of the important objectives of this benchmark study is to establish a reliable procedure for evaluating data obtained in the SODI. For this purpose, all the steps of the data extraction procedure are discussed in detail below.

3.1.1 Temperature records and experimental time-line

Software developed by QinetiQ Space (developer of the SODI instrument) records all the parameters that are vital for the proper execution of the experiments. Records of thermistors that control the temperatures of the copper blocks of the cell have particular importance for extracting scientific information. The data acquisition frequency was 2 Hz, providing approximately 74800 data points from each sensor during 623 min of the experimental run.

Correlation of the temperature record with the time stamps of acquired images allowed precise identification of the image that will be taken as the reference image and of the time margins for image sets attributed to a particular experimental step. Due to this correlation, an entire experimental run can be separated into three main steps.

1) Initial isothermal step to equilibrate the set-up and liquid at a constant temperature $T_0 = 298.15\,\text{K}$, which lasts 30 min. During this time, 19 stacks of interferograms were acquired equidistantly in time. Hereafter, *stack* refers to a specific set of 5 fringe images.

2) Soret separation step, which has the objective of measuring the separation of components driven by a temperature gradient. At the beginning of this step, set-points of $T_{\text{bot}} = T_0 - \Delta T/2$ and $T_{\text{top}} = T_0 + \Delta T/2$ were applied to the bottom and top plates, respectively. The imposed temperature difference of $\Delta T = 10.0\,\text{K}$ was kept constant over the entire step, but some minor fluctuations with a magnitude of 0.012 K (RMS value) were present due to active regulation. The duration of this step was 358 min, during which 161 stacks of interference patterns were acquired. The time step between acquired images was variable, changing from 5 s at the very beginning to 200 s at the end.

3) Diffusion relaxation step, when the temperature gradient is removed and both plates are held at the mean temperature. This step lasted 235 min, and the number of acquired stacks was 124. This last experimental step will not be considered in the current study.

3.1.2 Optical phase extraction

A phase-shifting technique was employed to determine the phase difference between a test beam and a reference beam using five successive images. The information needed to retrieve scientific data was kept in stacks (files with extension .stk). Each stack contained five interference patterns (fringe images) recorded by a CCD camera in RAW format for one laser. Each image was acquired at a particular value of the laser diode driving current. The stepwise variation of the laser current provides the wavelength shift and, consequently, the optical phase shift between subsequent interferograms within the stack. The typical time lag between the last and first interference patterns within a stack did not exceed 1 s, and it has no effect in a slow diffusion-controlled process. However, it might be important for the reconstruction of a correct optical phase at the temperature gradient build-up stage when the temperature rapidly varies.

To obtain the optical phase from the stack of interferograms we tested both the standard Hariharan's algorithm [8] and its modified version [14]. We finally selected the latter one and subsequently used it for phase extraction. The expression for the phase evaluation is as follows:

$$\phi(x,z) = \arctan \frac{7(I_4 - I_2)}{4I_1 - I_2 - 6I_3 - I_4 + 4I_5},$$

where the spatial coordinates of image intensities $I_i(x,z)$ are omitted for clarity.

All the stacks were processed into wrapped optical phase maps and stored in the computer for further processing as lossless bitmap images of 8 bit gray scale. This storage requires considerably less disk space compared with storing all the maps in double precision format. It does not reduce the accuracy of the data because the resulting resolution of the phase after such storage is $2\pi/256 = 0.025$ rad, which is essentially below the typical level of background noise observed on the phase maps.

3.1.3 Selecting the reference phase image

One of the important steps in obtaining correct results is the correct choice of the so-called reference phase image. This reference image will be subtracted from each of the following images to isolate the value of interest and to monitor its evolution. The selection of the reference image essentially follows the procedure described in [12].

We are interested in the change in the refractive index caused by the Soret effect. Thus, the reference image has to be chosen at the time instant when the thermal field is completely established inside the experimental cell. One of the easiest methods is to select this instant equal to the characteristic thermal time $\tau_{\text{th}} = H^2/\chi$, where χ is the thermal diffusivity of the liquid and H is the characteristic length (cell height). However, the temperature stabilization also depends on the time required by the temperature controllers to reach the set-point values, which is solely a technical constraint. Both factors, heat conduction and the response time of the temperature controllers, affect the thermal stabilization simultaneously, but based on our experience, the second factor is the most important. Therefore, a careful analysis of the actual temperature records is needed to select the proper reference image.

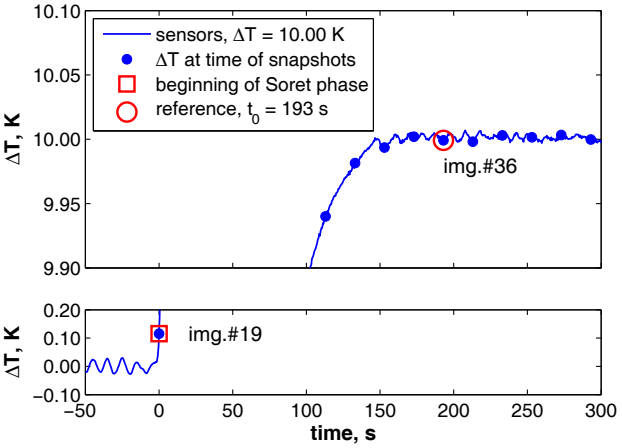

(a)

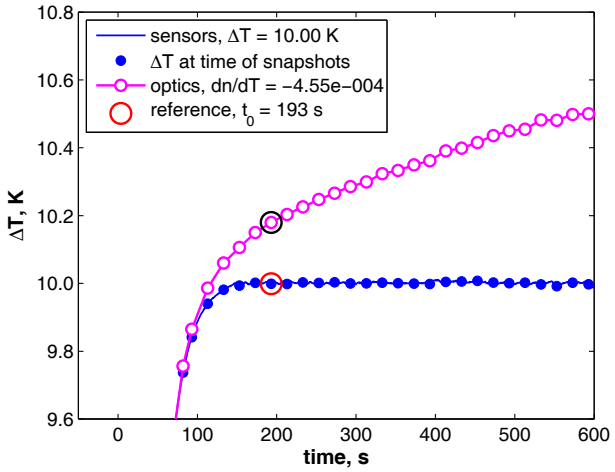

(b)

Fig. 2. Choice of reference image for processing of the Soret separation step.

Figure 2(a) shows the evolution of the temperature difference recorded by the sensors (solid curve) and the time instants of the snapshots (dots). Time zero was made to coincide with the boundary between step (1) and step (2), and it corresponds to image #19. The Soret step is started at this time instant by switching the temperature difference on. According to the records of the thermistors, complete temperature stabilization on both plates is attained at the moment when image #34 is acquired. With the purpose of reaching stabilization of the temperature field in the entire liquid volume, image #36 is selected as the reference image for final data extraction. The time difference between images #36 and #19 is $t_0 = 193$ s.

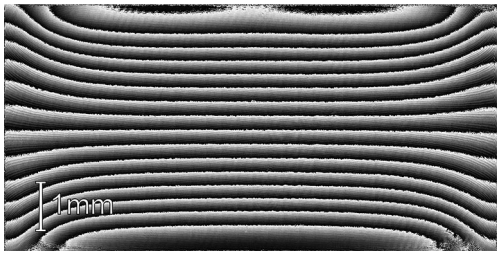

Fig. 3. Wrapped phase map after subtraction of the reference image obtained with the red laser, which corresponds to the end of the Soret separation phase.

Figure 2(b) compares ΔT recorded by the sensors (curve with closed circles) with the optically reconstructed ΔT across the cell (curve with open circles) using a reasonably adjusted value of the thermal contrast factor $(\partial n/\partial T)_{\mathrm{C}}$. Two large circles (red and black) indicate the position of the reference image in time, *i.e.*, $t = t_0$. The visible deviation of the optically evaluated temperature difference (black circle) from its real value (red circle) at $t = t_0$ indicates that the concentration separation occurs not only after but also before the reference image.

The optical contrast factors, used for data extraction from interferograms, $(\partial n/\partial T)$, $(\partial n/\partial C)$, depend on the temperature, concentrations, wavelength, etc. Hereafter, we will use their simplified notation without indicating by subscripts that all other parameters except for the main one, from which the derivative is calculated, are held constant.

3.1.4 Determination of refractive index profiles

After selection of two phase images, one to be processed and another as the reference, we have to subtract the reference phase image from the phase image of interest. Both of them are wrapped into $[0, 2\pi]$ range. It creates two options to proceed with processing. The first option is to independently unwrap both phase images and then to implement subtraction. The second option is to make subtraction first, then to wrap the result into the $[0, 2\pi]$ range, and only then to unwrap the single phase image. Both options provide identical result. The second option with minimized unwrapping workload was our final choice because the phase unwrapping is most computationally demanding part of the processing.

After subtraction of the reference phase image from all the phase images of interest, the obtained wrapped phase images were rotated 1.2° counter-clockwise, and then, the field of view (FOV) was cropped for further processing. This is performed to correct the slight misalignment between the camera and the cell. After cropping, all image regions related to the plates and side walls were removed, transforming the original size of the image from 1920×1080 pixels to 1530×765 pixels, which covers a FOV of exactly 10×5 mm. An example of a wrapped phase image obtained with the red laser at the end of the Soret step is presented in fig. 3.

The obtained phase maps were subjected to two-dimensional (2-D) phase unwrapping based on the simple pixel-to-pixel comparing principle but with a specifically oriented unwrapping path, starting from the region with the best phase quality toward regions with worse phase quality.

The unwrapped phase map was converted into a map of refractive index by applying the expression

$$n(x, z) = \frac{\lambda}{2\pi L}\phi(x, z), \tag{4}$$

where $L = 10.0$ mm is the path that the beam passes through in the liquid volume and λ is the wavelength.

Because the phase and, consequently, the refractive index obtained by eq. (4) suffer from absolute value ambiguity, the value of the refractive index has to be normalized. Subtraction of the refractive index value averaged over the FOV, $n'(x, z) = n(x, z) - \langle n(x, z)\rangle_{\mathrm{FOV}}$, is a convenient method for such normalization.

Then, the 1-D profile of a normalized refractive index along the diffusion path is determined from its 2-D map. For this purpose, a normalized refractive index is averaged in the horizontal direction within a selected vertical band/strip of pixels from the map. The bands/stripes of maps selected for averaging are shown in fig. 4(a) by dashed lines, and the arrows indicate regions and the direction of averaging. Figure 4(b), which shows the refractive index difference between the hot and cold walls, clarifies the selection principle. This is performed to avoid the impact of the corners of the cell with non-linear temperature on the resulting profile and to exclude the central region of the cell where the channel to the compensation volume is located. Thus, the visible reduction in the observed refractive index difference in these regions does not affect the final average result. The averaging increases the reliability of the extracted profiles because it suppresses local noise, which is otherwise observable, without applying additional filters.

3.1.5 Concentration separation during the temperature gradient build-up time

After cropping out Δn_Z in the problematic regions of the cell, the 1-D profile obtained by averaging from the 2-D map does not have the perfectly linear shape expected at steady state, as shown in fig. 4(c). It deviates from linearity, particularly at the boundaries. This result can be explained by fig. 2(b): at times earlier than the time of the reference image, the separation of components already occurs, and this separation begins near horizontal walls. However, subtraction of the reference image turns this contribution into background. The magnitude of this neglected separation depends on the values of the initial time t_0 (*i.e.*, the time between reference image and switching on of the temperature gradient) and on the diffusion coefficients, and as a rule, it is not very small.

Several approaches are available to overcome this problem, for example, restoring this missing separation by linear interpolation over the central part of the cell or cutting

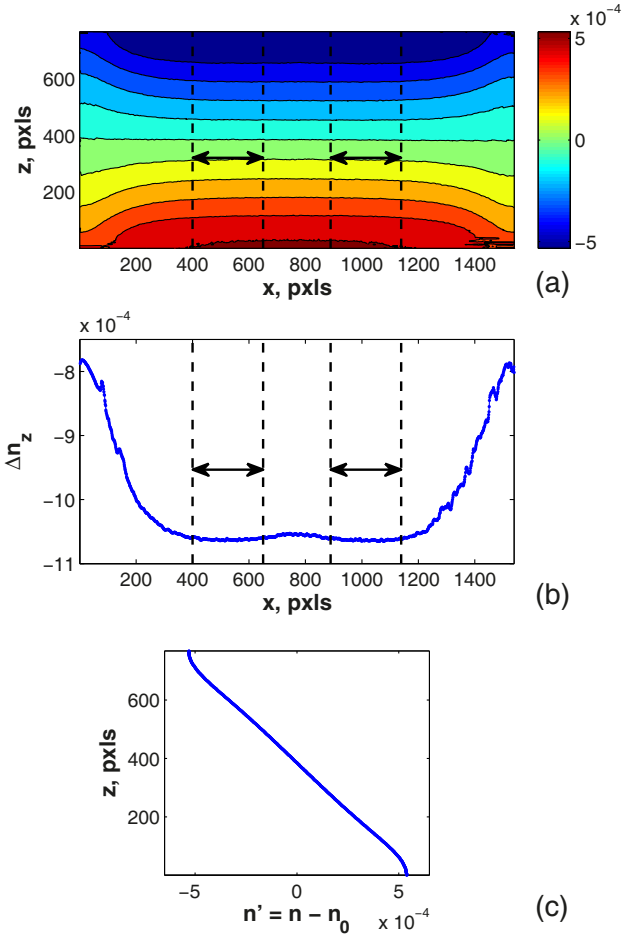

Fig. 4. Determination of 1-D profile of a refractive index from its 2-D map at the end of the Soret separation phase as observed by the red laser. (a) 2-D map of the normalized refractive index. (b) Refractive index difference between hot and cold walls. Dashed lines and arrows indicate regions remaining after cropping, inside which averaging is performed. (c) Resulting 1-D profile after averaging.

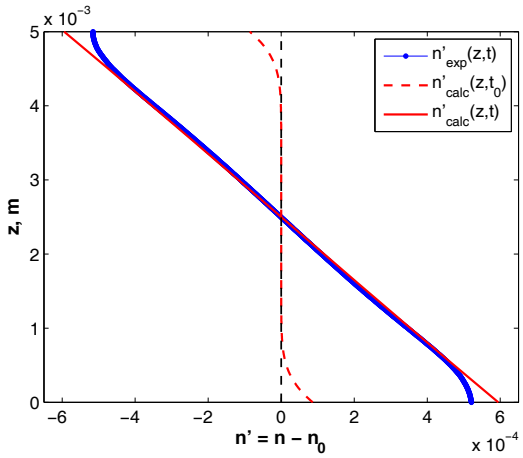

Fig. 5. Refractive index profiles, experimentally observed and analytically calculated, corresponding to different terms of the objective function eq. (5); blue dots represent the experimental profile, the dashed red line is the calculated profile of the initial time separation, and the solid red line is the calculated profile corresponding by time to the experimental one. The experimental profile is taken with red laser at the end of the Soret separation step.

out the central part of the profile, where the influence of the initial separation is not as noticeable.

A completely different approach is based on explicitly introducing the initial time t_0 into the fitting algorithm [12,15]. The objective function that has to be minimized during the course of the fitting takes the following form:

$$\Phi = \sum_{i,j} \left[n'_{\mathrm{exp}}(z_i, t_j) + n'_{\mathrm{calc}}(z_i, t_0) - n'_{\mathrm{calc}}(z_i, t_j) \right]^2, \quad (5)$$

where $t_{j=1} = t_0$. Here, an additional term is introduced into the objective function; this term corresponds to separation reached by the system at time instant t_0 according to the analytical model of separation (second term on the right-hand side of eq. (5)).

The results of this approach are shown in fig. 5, in which each of the three profiles corresponds to one of the terms in eq. (5). It is clearly observed (and effectively confirmed by values of the objective function) that adding the calculated profile corresponding to time t_0 to the experimental profile of any further time t_j will provide a much better fit to the full profile calculated for this time t_j. This approach does not require special consideration regarding the small magnitude of t_0 because it is already accurately accounted for. Furthermore, this approach has been systematically and successfully used for all of our previous ground measurements based on a similar technique [16,17].

An alternative approach would be to use direct numerical simulations in the fitting procedure rather than an analytical solution, see [18,19], although in the case of ternary mixtures, it is a computationally demanding task.

3.1.6 Two-parameter fit

The purpose of this section is to find true steady-state refractive index differences at each wavelength Δn_i^{st} and related concentration separations ΔC_i^{st}.

At this step, the ternary mixture is considered to be quasi-binary; subsequently, evolution of the component separation is characterized by a single diffusion coefficient, referred to as the effective diffusion coefficient, D_{eff}. The applicability of this approach follows from the expectation that the eigenvalues of a diffusion matrix for the ternary system are rather close.

In this case, the analytical profiles are calculated using

$$n'(z,t) = \Delta n^{\mathrm{st}} \cdot f(z, t, D_{\mathrm{eff}}), \quad (6)$$

where $f(z,t,D)$ is the function presenting the solution of the diffusion problem with initial and boundary conditions of the Soret cell for the case of a binary mixture. The

Table 1. Optical contrast factors taken from [20].

wavelength	$\left(\frac{\partial n}{\partial C_{\mathrm{THN}}}\right)$	$\left(\frac{\partial n}{\partial C_{\mathrm{IBB}}}\right)$
670 nm	0.142741	0.088676
925 nm	0.137344	0.083753

expression for the function is

$$f(z,t,D) = \frac{1}{2} - \frac{z}{H} - \frac{4}{\pi^2}\sum_{k,\mathrm{odd}}^{\infty}\frac{1}{k^2}\cos\left(\frac{k\pi z}{H}\right)\exp\left(-\frac{k^2\pi^2}{H^2}Dt\right). \tag{7}$$

The fitting procedure with the use of eq. (6) comprises two fitting parameters: Δn^{st} and D_{eff}.

The fitting of two datasets related to different lasers is performed independently, and it provides two stationary values: $\Delta n^{\mathrm{st}}_{670\,\mathrm{nm}}$ and $\Delta n^{\mathrm{st}}_{935\,\mathrm{nm}}$. These variations in the measured refractive indices allow the variation in concentrations to be determined through solving a system of linear equations

$$\begin{pmatrix}\Delta n_1^{\mathrm{st}}\\ \Delta n_2^{\mathrm{st}}\end{pmatrix} = \begin{bmatrix}\left(\frac{\partial n_1}{\partial C_1}\right) & \left(\frac{\partial n_1}{\partial C_2}\right)\\ \left(\frac{\partial n_2}{\partial C_1}\right) & \left(\frac{\partial n_2}{\partial C_2}\right)\end{bmatrix}\begin{pmatrix}\Delta C_1^{\mathrm{st}}\\ \Delta C_2^{\mathrm{st}}\end{pmatrix} = [A]\begin{pmatrix}\Delta C_1^{\mathrm{st}}\\ \Delta C_2^{\mathrm{st}}\end{pmatrix}. \tag{8}$$

The optical contrast factors $(\partial n_i/\partial C_j)$ composing matrix $[A]$ in eq. (8) were obtained from interpolating polynomials eqs. (1)-(2) in [20] for wavelengths of 670 and 925 nm, and their values are given in table 1.

3.1.7 Six-parameter fit

A more general and correct approach is to consider the full problem that takes into account the complete diffusion matrix. In ternary mixtures, two concentration variations independently contribute to the variation in the refractive index:

$$n_j'(z,t) = \left(\frac{\partial n_j}{\partial C_1}\right)_{C_2,\lambda_j} C_1'(z,t) + \left(\frac{\partial n_j}{\partial C_2}\right)_{C_1,\lambda_j} C_2'(z,t), \tag{9}$$

where $C_i'(z,t) = C_i(z,t) - C_i^0$ is the variation of the i-th component with respect to its initial value C_i^0 and j indicates the laser.

To fit the experimental $n'(z,t)$ profiles to eq. (9), an analytical solution is needed for both concentrations. By using the diffusion matrix diagonalization method [21], the solution can be written as

$$\begin{pmatrix}C_1'(z,t)\\ C_2'(z,t)\end{pmatrix} = [B]\cdot\begin{bmatrix}f_1 & 0\\ 0 & f_2\end{bmatrix}\cdot[B]^{-1}\cdot\begin{pmatrix}\Delta C_1^{\mathrm{st}}\\ \Delta C_2^{\mathrm{st}}\end{pmatrix}, \tag{10}$$

where the modal matrix $[B]$ is defined as

$$[B] = \begin{bmatrix}1 & 1\\ v_1 & v_2\end{bmatrix} = \begin{bmatrix}1 & 1\\ \frac{\hat{D}_1 - D_{11}}{D_{12}} & \frac{\hat{D}_2 - D_{11}}{D_{12}}\end{bmatrix}. \tag{11}$$

Here, D_{ij} are the elements of a diffusion matrix; $\hat{D}_i$ are the eigenvalues of a diffusion matrix; v_1 and v_2 are the eigenvectors; and the functions $f_i = f(z,t,\hat{D}_i)$ are the same as those given by eq. (7).

Then, the solution for the concentration profiles obtained by eqs. (10)–(11) and the function from eq. (7) are substituted into eq. (9) and fitted to the experimental data. In this case, there are six parameters to fit: two eigenvalues, $\hat{D}_1$ and $\hat{D}_2$, two eigenvectors, v_1 and v_2, and two stationary concentration separations, ΔC_1^{st} and ΔC_2^{st}.

The problem of initial time t_0 is equally valid for this data extraction approach, although in this case, the accounting for the initial time is generally more correct because both kinetics are properly defined by two eigenvalues. The Nelder-Mead and Levengergh-Marquardt fitting techniques are used. The latter was tested with both numerically calculated and analytically expressed Jacobian matrices.

3.1.8 Uncertainty caused by non-linear temperature field

The temperature field in the cell is spatially non-linear, and it causes the non-linearity of the refractive index distribution, as shown in figs. 3, 4. Consequently, a concentration field obtained via the refractive index variation exhibits similar non-linearity. Optical integration of such a deformed field leads to an underestimated value of the Soret separation ΔC_i between differently heated walls [7].

An important starting point for the determination of the correct profile from the disturbed picture is to apply tomography reconstruction of the 3-D concentration field in the whole cell. Of course, one view provided by the interferometer is not sufficient for such a reconstruction. A second view of the cell, identical to the basic one (see fig. 6(a)), can be assumed keeping in mind the square symmetry of the cell. Two views are sufficient for robust reconstruction following the algebraic algorithm suggested in [22]. A target of the reconstruction is just one vertical line, located in the cell center (dashed red line in fig. 6(a)). On that line, both the temperature and concentration profiles are less perturbed by disturbances originating from the cell corners and are expected to be closest to linear.

The algorithm of the reconstruction is as follows: from the 2-D map, we select the i-th row of pixels/points with n values of refractive index, from $n_{i,1}^{(1)}$ to $n_{i,n}^{(1)}$; see fig. 6(b). Here, the superscript $^{(1)}$ means that these values relate to the 1st view. The same i-th row of pixels from the second view (superscript $^{(2)}$) also participates in the reconstruction. The reconstruction proceeds in a row-by-row manner.

Processing begins from an initial guess that assigns some average value to all 3-D cells n_{ikl} whose values are

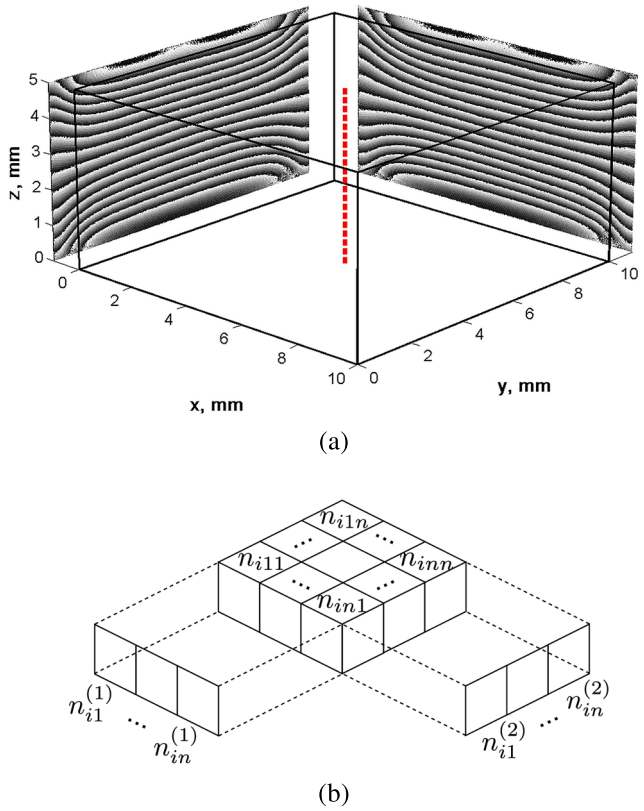

Fig. 6. Schematic representation of the tomography reconstruction concept (a) and illustration of the algorithm procedure (b).

the target of the reconstruction. Then, all values of cells from n_{i11} to n_{i1n} are proportionally corrected in such a way to obtain an integral (arithmetic average) of them equal to a pixel value of $n_{i,1}^{(1)}$. The same procedure is applied to all rows until the end, which corresponds to pixel $n_{i,n}^{(1)}$. Afterwards, the values of the 3-D cells allow the first view to be perfectly reconstructed, although the second view will appear out of range after this procedure.

Logically, the same procedure is applied for the second view; in particular, all values of cells from n_{i11} to n_{in1} are proportionally corrected in such a way to obtain the integral of them equal to a pixel value of $n_{i,1}^{(2)}$. The procedure is repeated until the row corresponding to the last pixel $n_{i,n}^{(2)}$. Such processing with alternating views is repeated in a loop until convergence to a given tolerance of the values of 3-D cells is reached.

This procedure allows the refractive index profile along the cell center to be restored with reduced impact from the grooves at the lateral walls and deformations at the corners. However, it reveals the influence of the compensation volume in a most pronounced manner.

3.1.9 Uncertainty caused by compensation volume

Careful examination of the refractive index profiles reveals slight non-symmetry between the top and bottom parts. The wrapped phase map in fig. 3 presents clear evidence

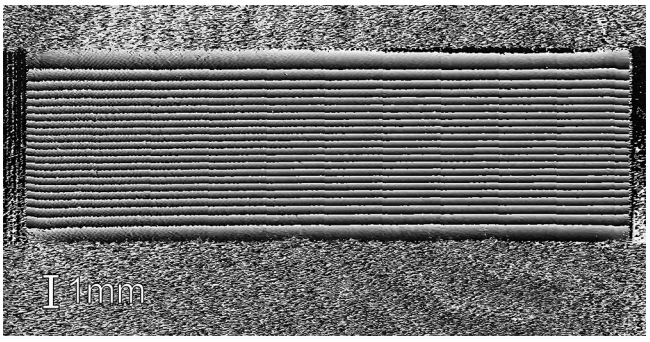

Fig. 7. Wrapped phase map obtained at the end of the Soret phase in the ground set-up.

of the fringe perturbations at the middle of the top plate caused by the presence of a compensation volume. The reconstructed 3-D distribution exhibits the same feature (fig. 9).

The simplest (but, it appears, most exact) approach to remove this concern is to limit the fitting area only to the bottom half of the cell, to $0 \leq z \leq H/2$.

3.2 Extraction of the Soret coefficients in the ground ODI set-up

Because SODI and ground ODI instruments are based on the same principle, most of the data analysis steps are equivalent. Thus, in this section, we will only point out the differences between them.

A peculiarity of the ground interferometer is that it is aligned for obtaining narrow fringe patterns, and it utilizes the 2-D Fourier transform technique to extract optical phase information from interferograms (see a detailed description of the technique in [12]). In this case, all spatial information is obtained instantly from a single snapshot, and therefore, the result is not sensitive to how fast the variation in the refractive index is inside the cell.

The correct choice of a reference phase image is equally important for the laboratory set-up and for its on-board analogue. In the laboratory set-up, the initial time value is different and is typically equal to $t_0 = 400$–600 s, although the approach for finding this time is exactly the same as that discussed in sect. 3.1.3. The large difference in the initial time t_0 between the two experiments can partly be attributed to the different thermal characteristic times of the cells. Because the height of the cells is different (6.06 mm *versus* 5 mm), τ_{th}^{lab} is approximately 1.5 times larger than τ_{th}^{ISS}. However, it does not explain the complete difference that is, mostly, attributed to various response times of the thermal regulation system.

The important difference between the two instruments is the design of the experimental cell. The cell of the ground set-up has passed a long chain of improvements (see, *e.g.* [15]), and as a result, the thermal and concentration fields in the cell are not disturbed by lateral walls. The distribution of refractive indices associated with the concentration field has a perfect 1-dimensional character, as shown in fig. 7; subsequently, the analysis of the ground

results does not require the steps discussed in sects. 3.1.8, 3.1.9 (tomography reconstruction and consideration of the parasitic mass flux from compensation volume).

3.3 Measurement of diffusion coefficients by the Taylor Dispersion Technique (TDT)

To characterize the diffusion matrix using the Taylor Dispersion Technique (see a description of the instrument in [13]), small injections of three different concentrations into the laminar flow of a carrier solution inside a thin long capillary were performed. The concentration of the diffusing injected samples as a function of time was monitored at the end of the capillary using a high-sensitivity differential refractometer. The recorded curve is very close to a Gaussian function in the case of binary solutions. The width of the peak is defined by a diffusion coefficient, and for a binary solution, it is determined even by a single experiment.

In the case of a ternary solution, two Gaussian functions are mixed together. They may have very different amplitudes and peak widths (defined by eigenvalues of the diffusion matrix), sometimes forming very complex signal shapes. A set of experiments with injections of different concentrations is required to obtain reliable results. In the particular case when the eigenvalues are similar in magnitude, resolving them by fitting an experimental signal becomes very challenging.

Important steps of data processing also include preparing the signals to fit (baseline subtraction) and estimating the so-called sensitivity ratio, which is the ratio of the detector's sensitivities to changes in two independent concentrations. Details on these steps, as well as formulations for the analytical model of signals for the case of ternary mixtures, are given in [23].

4 Results

4.1 Soret coefficients from microgravity experiment

In this section, we present the results from the analysis of the microgravity experiment. As we have noted, the complete procedure consists of several steps and implements some data corrections. To illustrate the relative importance of different processing steps/corrections, all the results, including intermediate ones, will be presented in one table (table 2).

First, we analyzed refractive index variations obtained using the steps described in sects. 3.1.2–3.1.4. The results, obtained without accounting for the initial time and without any additional corrections, are listed in the very first row of table 2, and they form the starting point for further processing.

4.1.1 Two-parameter fit

The objective of this step is to find the true steady-state from the time-dependent behavior taking into account the separation lost at the initial time $t < t_0$. Raw profiles of the refractive index (obtained in sect. 3.1.4) were subjected to a two-parameter fit to extract stationary refractive index variations (as described in sects. 3.1.5–3.1.6).

Table 2. Separations as measured by refractive index. DCMIX-1 experiment, cell 3, run #18.

Processing stage	$\Delta n^{\mathrm{st}}_{670\,\mathrm{nm}}$, 10^{-4}	$\Delta n^{\mathrm{st}}_{935\,\mathrm{nm}}$, 10^{-4}	gain
(1) Separation visible from raw profiles	−10.704	−10.489	–
(2) Separation obtained by fitting profiles in transient with counting t_0	−12.196	−11.868	12-13%
(3) Separation obtained by fitting tomographically reconstructed profiles in transient	−13.217	−12.851	8%
(4) Separation from fitting bottom half of reconstructed profiles in transient	−13.485	−13.095	2%

We found that the initial time t_0^* used for fitting cannot be exactly equal to the time difference between the moment of switching the temperature difference on and the reference image #36. In theory, at the time $t = 0$, the temperature difference instantly jumps from zero to 10 K. In practice, at this moment, the temperature difference only began to increase with a finite rate. This is why the correct initial time should be $t_0^* < t_0$, which is indicated in sect. 3.1.3. To make the approach more reasonable, the zero time was shifted from the moment of imposing ΔT to the moment when the temperature difference recorded by the sensors reached $\Delta T/2$. Analysis of the temperature records reveals that it occurs at $t \approx 18$ s. Thus, the initial time used for calculation of the objective function was $t_0^* = t_0 - 18\,\mathrm{s} = 193 - 18 = 175\,\mathrm{s}$.

Figure 8 presents vertical profiles of the refractive index, both experimental and calculated according to the best fit, obtained after this processing step. Data points closest to the horizontal walls (2% of the diffusion path H on each side) were excluded from the fit to reduce noise from diffraction.

The resulting values of Δn_i^{st} are given in the second row of table 2. Note that the effective diffusion coefficient obtained by the fit was the same for both lasers,

$$D_{\mathrm{eff}} = 5.74 \cdot 10^{-10}\,\mathrm{m}^2/\mathrm{s}.$$

As shown in table 2, consideration of the initial time t_0 allows a gain of 13% for Δn_i^{st}, and as such, it has to be included as a necessary step in any data analysis.

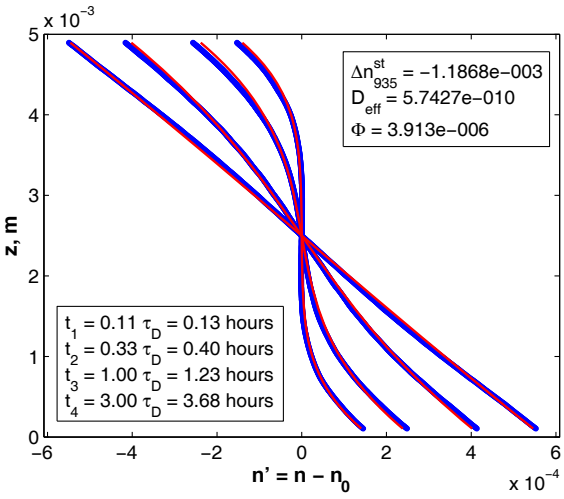

Fig. 8. Experimental (blue) and analytical (red) refractive index profiles at different time instants of the experiment after a quasi-binary two-parameter fit. Time is normalized by the diffusion time $\tau_D = H^2/(\pi^2 D_{\text{eff}})$.

Then, ΔC_i^{st} can be determined by solving a system of equations (8) with the contrast factors from table 1. Using the measured refractive index differences Δn_i^{st}, the solution provides the required concentration separations ΔC_i^{st} (in mass fraction):

$$\Delta C_{\text{THN}}^{\text{st}} = -1.381 \cdot 10^{-2}, \qquad \Delta C_{\text{IBB}}^{\text{st}} = 0.848 \cdot 10^{-2}.$$

4.1.2 Six-parameter fit

This fit is performed simultaneously with data from both lasers being aimed to simultaneously extract six independent parameters, as described in sect. 3.1.7. Contrast factors, the same as in the previous step, are the constant parameters given in table 1.

To investigate the robustness of the fit, the set of initial guesses were tested with different but physically meaningful values. The results of the fitting runs were somewhat scattered and can be summarized as follows. Eigenvalues are the most robust group of parameters; they always converged to the same values

$$\hat{D}_1 = 6.81 \cdot 10^{-10} \qquad \text{and} \qquad \hat{D}_2 = 0.75 \cdot 10^{-10}\,\text{m}^2/\text{s}.$$

Next, less robust are the concentration separations; although varying, they always remained within the limits

$$\Delta C_{\text{THN}}^{\text{st}} = (-1.5 \pm 0.15) \cdot 10^{-2},$$
$$\Delta C_{\text{IBB}}^{\text{st}} = (0.8 \pm 0.2) \cdot 10^{-2}.$$

Finally, components of eigenvectors v_i exhibited non-systematic scattering.

Notably, substituting essentially scattered values of ΔC_i^{st} in eq. (9) provides values Δn_i^{st} that are consistent with those provided by the two-parameter fit, although they are slightly overestimated. The reason for this overestimation is attributed to the small value of the second eigenvalue defined by the multi-parameter fit. Due to the presence of the unrealistically slow second kinetics, the analytical solution would reach a true steady-state 10–15 times later than in the real experiment and would provide a greater value. Because such small eigenvalues should be considered as a mathematical phantom rather than as a real physical property of the system, this overestimation is non-physical.

We can conclude that the six-parameter fit cannot be considered reliable because of the large number of unknowns and the high sensitivity to the imperfection of the experimental data. However, this fit confirms quite well the results of the steady separation obtained by the quasi-binary fit. Thus, in further analyses, we will use only the two-parameter quasi-binary fit because it is considerably more robust, less computationally demanding and confirmed to be accurate.

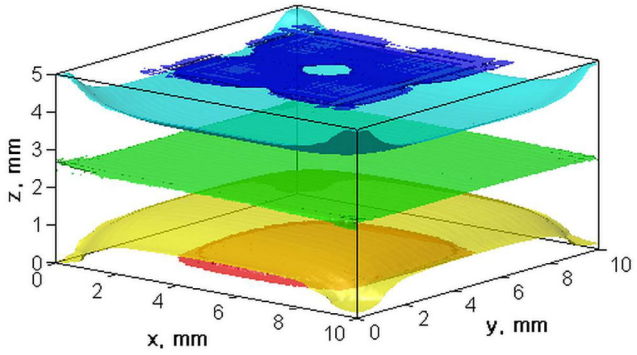

Fig. 9. Refractive index field at the end of the Soret step reconstructed by the tomography.

4.1.3 Result of tomography reconstruction

Here, the tomography reconstruction of the refractive index distribution inside the mixture is applied as described in sect. 3.1.8. To perform the reconstruction of all available 2-D maps in a reasonable amount of time, we rescaled these maps from 1530×765 points to 201×101 points by linear interpolation. This change of the scale keeps a reasonable compromise between computation cost and data resolution.

The result of the tomography reconstruction at the end of the Soret step is shown in fig. 9 with spacing between iso-surfaces $\Delta n = 2.75 \cdot 10^{-4}$. Strong 3-D deformation of the field is clearly visible: bending of iso-surfaces at the corners reflects nonlinearity of the thermal field, and a circular hole in the center of the top iso-surface (blue) shows the effect of the compensation volume.

A refractive index profile taken from these 3-D distributions exhibits deviation from the original profile taken from the 2-D map, as shown in fig. 10. As expected, the refractive index variation over the height of the cell is larger in the reconstructed profile. All reconstructed profiles were subjected to the two-parameter fit. The steady refractive

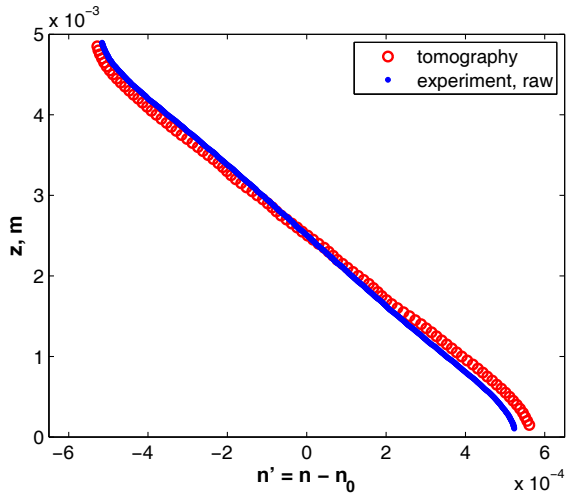

Fig. 10. Comparison of refractive index profiles obtained from integrated 2-D refractive index map (blue dots) and from 3-D distribution along the centerline of the cell (red circles).

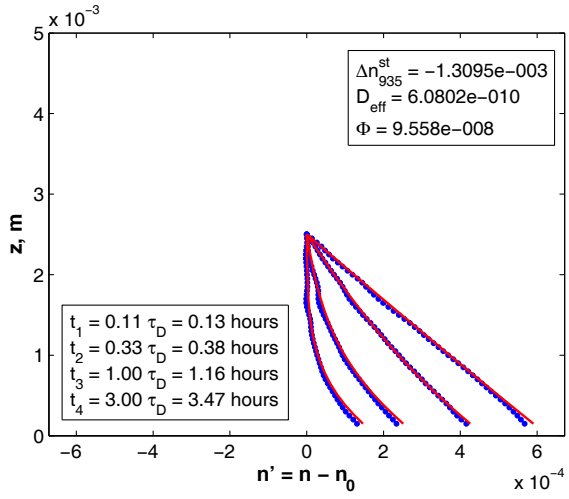

Fig. 11. Experimental and analytical refractive index profiles at different time instants of the experiment after a quasi-binary two-parameter fit in the bottom part of the cell.

index differences Δn_i^{st} after this correction are given in row (3) of table 2. The increase in separation achieved at this step is 8%.

4.1.4 Correction attributed to compensation volume

Tomography reconstruction allows the missing separation due to disturbances from lateral walls and corners to be retrieved. At the same time, however, this profile is mostly exposed to the influence of the compensation volume, whose channel is located in the center of the top plate.

The effect from this channel is mostly localized in the upper half of the cell, close to the channel position. Therefore, a logical solution is to cut and crop out the top part of the profile. The fit is performed with the residual part of all the profiles, *i.e.*, within $0 \leq z \leq H/2$.

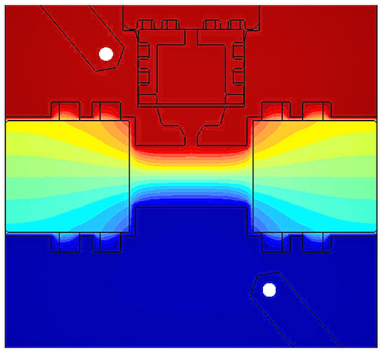

Fig. 12. Computed temperature field in the geometry of the experimental cell. White spots indicate the positions of the sensors.

The qualitative results of the fit after cropping are shown in fig. 11, and the quantitative results are given in the fourth row of table 2. Compared with previous steps, the gain achieved here is not large, approximately 2%. However, considering the poor conditioning of the matrix of contrast factors, even a tiny error in measured Δn can produce a large shift of the solution for concentration separations. This is why if correction is possible, it has to be implemented.

Finally, note that the last values of Δn_i^{st} given in row (4) of table 2 will be used for calculating the Soret coefficients.

4.1.5 Correction of temperature difference

Another issue that may slightly affect the values of the Soret coefficients is the temperature difference used for the calculation of these coefficients. In reality, the temperature difference, which is assumed to be between the working surfaces of the copper blocks, corresponds to the temperature difference between the positions of the sensors inside these blocks. The actual position of the sensor is at least a few millimeters out of the working surface of the block, and this may introduce a certain misfit between ΔT displayed by the sensors and the actual temperature difference that drives Soret separation.

To estimate the effect of the position of the sensors on the temperature difference, 2-D stationary heat transfer calculations were conducted using the *Comsol Multiphysics* package with the correct cell geometry, material properties and realistic boundary conditions.

The computed temperature field is presented in fig. 12. Constant temperature boundary conditions for the outer limits of the copper blocks were adjusted in such a way to have the exact values given by the sensors indicated by white spots in the figure.

While the calculated temperatures at the locations of the sensors perfectly reproduce the values provided by the measurements, the temperature difference between the working surfaces of the plates does not provide the same value. The temperature slightly changes over the surface, but on average, the temperature difference between sen-

Table 3. Results of ground experiments, $\Delta T = 5.994$.

run (#)	λ (nm)	$\Delta n^{\rm st} \cdot 10^4$	$-\frac{\Delta n^{\rm st}}{\Delta T} \cdot 10^4$ ($\rm K^{-1}$)	$D_{\rm eff} \cdot 10^{10}$ ($\rm m^2/s$)
1	670	−8.3763	1.3974	5.65
2	670	−8.3664	1.3958	5.72
3	670	−8.3473	1.3926	5.69
		−8.3633	1.3953	
		±0.0147	±0.0025	
4	925	−8.0441	1.3420	5.63
5	925	−8.0726	1.3468	5.67
6	925	−8.0502	1.3430	5.63
		−8.0557	1.3440	
		±0.0150	±0.0025	

sors $\Delta T_{\rm sensor} = 10.0\,\rm K$ corresponds to $\Delta T = 9.95\,\rm K$ between the surfaces of the plates. This reduced temperature difference will be used for calculating the Soret coefficients.

4.1.6 Soret coefficients

By solving a system of linear equations (8) with the matrix of optical contrast factors $[A]$ with elements from table 1 and the measured refractive index differences $\Delta n_i^{\rm st}$ from the last row of table 2, we obtain the required concentration separations $\Delta C_i^{\rm st}$ (in mass fraction):

$$\Delta C_{\rm THN}^{\rm st} = -1.419 \cdot 10^{-2}, \qquad \Delta C_{\rm IBB}^{\rm st} = 0.763 \cdot 10^{-2}.$$

After dividing by $\Delta T = 9.95\,\rm K$, these separations provide the desired Soret coefficients

$$S'_{T,1}({\rm THN}) = 1.426 \cdot 10^{-3},$$
$$S'_{T,2}({\rm IBB}) = -0.767 \cdot 10^{-3}\,\rm K^{-1}.$$

The value of Soret coefficient for third component can also be found due to the mass conservation that requires vanishing of the sum of Soret coefficients for all three components

$$S'_{T,3}(n{\rm C}_{12}) = -0.659 \cdot 10^{-3}\,\rm K^{-1}.$$

4.2 Soret coefficients from the ground experiment

Data from ground experiments were processed using the procedure discussed in sects. 3.1.2–3.1.4 to obtain normalized refractive index profiles, and then, two-parameter fits were used to obtain steady refractive index differences, as described in sects. 3.1.5–3.1.6. The results from all the experiments are summarized in table 3.

Because the experiment was repeated several times, we were able to determine the standard deviation for these refractive index differences. This error will allow us to estimate the overall precision of the derived Soret coefficients.

Table 4. Comparison of normalized refractive index differences obtained in microgravity (without and with all corrections) and in ground experiments.

Experiment	$-\frac{\Delta n_1^{\rm st}}{\Delta T} \cdot 10^4$ ($\rm K^{-1}$)	$-\frac{\Delta n_2^{\rm st}}{\Delta T} \cdot 10^4$ ($\rm K^{-1}$)
Microgravity, row (2) of table 2	1.226	1.193
Microgravity, row (4) of table 2	1.355	1.316
Ground	1.3953 ±0.0025	1.3440 ±0.0025

Remarkably, the repeatability of the measured $\Delta n_i^{\rm st}$ is excellent, exhibiting a dispersion of only 0.2%. The actual temperature difference in the ground experiments was also verified by calculating the heat transfer in the actual geometry of the cell, and it was $\Delta T = 5.994\,\rm K$.

Direct comparison of $\Delta n^{\rm st}$ observed in the experiments with different ΔT (as in the case with the experiments performed in the SODI and in the ground ODI) is not possible. It is convenient to introduce the variation of the refractive index per 1 K of temperature difference, so we introduce the parameter $-\Delta n_i^{\rm st}/\Delta T$.

A comparison of space and ground results by this normalized parameter is given in table 4. In the case when tomography reconstruction and correction for the compensation volume are not implemented (first row in table 4), the microgravity results deviate from the terrestrial ones. Analysis of the microgravity results with all the necessary corrections (second row in table 4) provides much better agreement between these two experiments. Note that the agreement between the effective diffusion coefficients found in terrestrial and microgravity experiments was good.

The Soret coefficients can be determined from the steady-state measurements and the matrix of contrast factors according to the equations

$$\begin{pmatrix} S'_{T,1} \\ S'_{T,2} \end{pmatrix} = -\frac{1}{\Delta T}\,[A]^{-1} \begin{pmatrix} \Delta n_1^{\rm st} \\ \Delta n_2^{\rm st} \end{pmatrix}. \qquad (12)$$

The calculated Soret coefficients for ground experiments from the data presented in table 3 are as follows:

$$S'_{T,1}({\rm THN}) = 1.035 \cdot 10^{-3},$$
$$S'_{T,2}({\rm IBB}) = -0.093 \cdot 10^{-3}\,\rm K^{-1},$$

and for the third component

$$S'_{T,3}(n{\rm C}_{12}) = -0.942 \cdot 10^{-3}\,\rm K^{-1}.$$

4.3 Error estimation

Error estimation for Soret coefficients in ternary mixtures from optical measurements has a certain peculiarity. It can

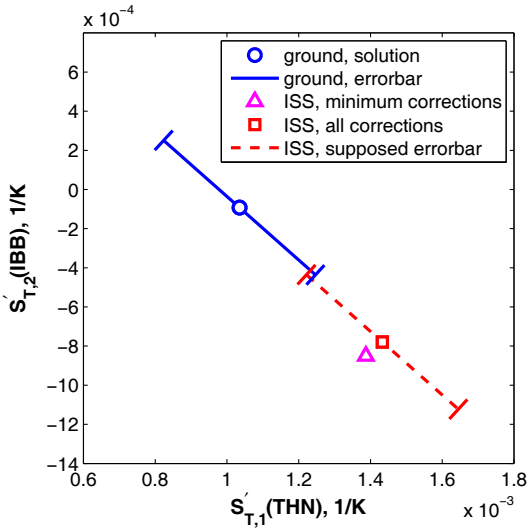

Fig. 13. Summary of the Soret coefficients measured in microgravity and ground instruments.

be examined by dividing the data analysis into two steps: the *measurement* step and the *calculation* step. During the measurement step, after several repetitions of the experiment, the mean values of Δn_1, Δn_2 and their standard deviations $\sigma_{\Delta n_1}$, $\sigma_{\Delta n_1}$ can be evaluated. In the first approximation, these two standard deviations can be considered as independent from each other. They are rather small; our results with ground experiments show that for steady state $\sigma_{\Delta n_i^{\rm st}} \approx 0.015 \cdot 10^{-4}$.

At the *calculation* step, the measured quantities have to be recalculated into the desired coefficients. The Soret coefficients $S_{T,i}$ (and their errors) can be determined from the steady-state measurements as follows:

$$\begin{pmatrix} S'_{T,1} \pm \sigma_{S'_{T,1}} \\ S'_{T,2} \pm \sigma_{S'_{T,2}} \end{pmatrix} = -\frac{1}{\Delta T}\,[A]^{-1} \begin{pmatrix} \Delta n_1^{\rm st} \pm \sigma_{\Delta n_1} \\ \Delta n_2^{\rm st} \pm \sigma_{\Delta n_2} \end{pmatrix}, \quad (13)$$

where the values $\Delta n_i^{\rm st}$ correspond to the average values over a series of experimental runs. Here, we do not consider the error related to the measurements of the elements of matrix $[A]$.

The magnitude of the error of $S_{T,i}$ will appear as the value of the error of $\Delta n_i^{\rm st}$ magnified by the condition number of matrix $[A]$, which is large, $K = 241$. Solving the system of eqs. (13), we obtain the coordinates of the four points, limiting the area where the solution can be found. This area, forming a type of elongated parallelogram, is the error bar that bounds the possible solutions. The peculiar feature of this parallelogram is that one diagonal is much smaller than other one, and practically, it transforms into the line shown in fig. 13. The distinction of this error bar is that it relates to the solution of eqs. (13), *i.e.*, to the couple ($S_{T,1}$, $S_{T,2}$) but not to their *individual* values.

The orientation of the error bar is primarily defined by the matrix of the optical contrast factors; therefore, all results obtained with the same matrix should have an error bar with the same orientation. This orientation can be represented mathematically as an equation of a line passing through two extremities of the error bar:

$$S'_{T,1} = 0.972 \cdot 10^{-3} - 0.616 \cdot S'_{T,2}\,{\rm K}^{-1}.$$

This statement is also valid for measurements performed by the SODI instrument and presented in sect. 4.1.6. All the results obtained in microgravity and in ground laboratory are summarized in fig. 13. The magnitude of the error bar for the microgravity experiment can not be estimated from a single experimental run, but we may assume similarity of span of error bar relying on similarity of both experiments. This supposed error bar is plotted in fig. 13 by dashed red line. From the figure it follows that error bars of both ground and microgravity experiments do intersect, thus proving agreement of the results.

Figure 13 shows also that the only results of the microgravity experiment with all corrections agree with the ground experiment, whereas the results of processing with minimal correction are shifted out.

Table 5. Concentration of solutions used for Taylor dispersion measurements, in mass fractions.

Solution	$C_{\rm THN}$	$C_{\rm IBB}$	no. of runs
Carrier	0.79975	0.10023	–
Inj. 1	0.76010	0.14007	4
Inj. 2	0.76051	0.09980	3
Inj. 3	0.79996	0.14019	4

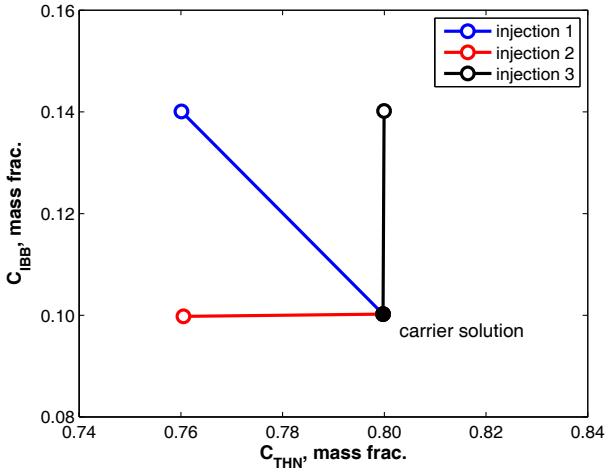

Fig. 14. Graphical representation of carrier and injected liquids in a space of independent concentrations.

4.4 Diffusion coefficients from TDT

Ternary dispersion profiles are generated by injecting small samples of a mixture containing components 1 (THN) and 2 (IBB) with mass fractions ($C_1^0 \pm \delta C_1$) and ($C_2^0 \pm \delta C_2$) into the carrier liquid of composition C_1^0 and

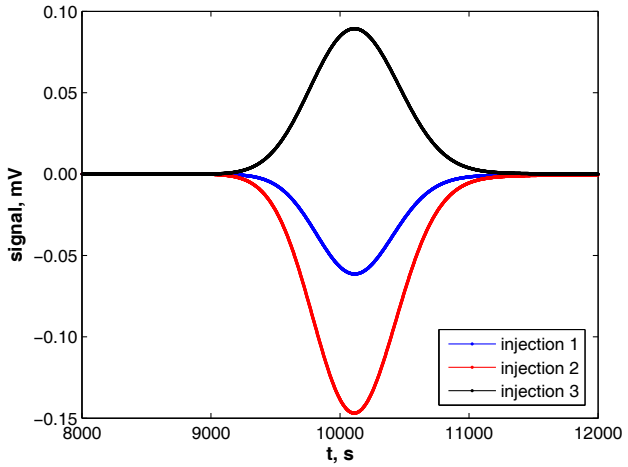

Fig. 15. Examples of peaks corresponding to different injected solutions.

C_2^0. For the benchmark mixture, 11 successive runs with injections of three different solutions, close but distinct from the carrier one, were performed to measure the diffusion coefficients. A list of injected solutions is given in table 5, and they are graphically represented in fig. 14. Ternary dispersion profiles (peaks) corresponding to these injections are presented in fig. 15.

The diffusion matrix obtained by simultaneous fitting of all Taylor dispersion runs is as follows:

$$D = \begin{bmatrix} 6.61 & -0.59 \\ -1.55 & 5.98 \end{bmatrix} \cdot 10^{-10}\,\mathrm{m}^2/\mathrm{s}, \qquad (14)$$

with eigenvalues of

$$\hat{D}_1 = 5.29 \cdot 10^{-10} \quad \text{and} \quad \hat{D}_2 = 7.30 \cdot 10^{-10}\,\mathrm{m}^2/\mathrm{s}.$$

An important fact in support of the previous examination of the two-parameter fit is that the two eigenvalues are rather close. Furthermore, one of the eigenvalues is close to the effective diffusion coefficient as well as to one of the eigenvalues obtained in the Soret experiments.

Several repetitions of each injection allow us to estimate error bars for the diffusion coefficients. For this purpose, we fit not all 11 runs but different combinations of 3 runs, each corresponding to a particular injection. Forty-eight different combinations of this type are possible among the list of runs given in table 5. It allows us to make a statistical estimation of the dispersion of the coefficients.

The standard deviations of all individual diffusion coefficients and eigenvalues are calculated as

$$\sigma_{D_{ij}} = \begin{bmatrix} \sigma_{D_{11}} & \sigma_{D_{12}} \\ \sigma_{D_{21}} & \sigma_{D_{22}} \end{bmatrix} = \begin{bmatrix} 1.5 & 91 \\ 6.5 & 7.3 \end{bmatrix} \%$$

and

$$\sigma_{\hat{D}_i} = \begin{pmatrix} \sigma_{\hat{D}_1} \\ \sigma_{\hat{D}_2} \end{pmatrix} = \begin{pmatrix} 1.7 \\ 3.5 \end{pmatrix} \%.$$

As expected, the dispersion is largest for cross-diagonal elements and smallest for eigenvalues of the diffusion matrix.

4.5 Thermodiffusion coefficients

Because the Soret and diffusion coefficients were independently measured, we can also estimate the thermodiffusion coefficients. These coefficients can be determined using equation

$$\begin{pmatrix} D'_{T,1} \\ D'_{T,2} \end{pmatrix} = [D] \cdot \begin{pmatrix} S'_{T,1} \\ S'_{T,2} \end{pmatrix}, \qquad (15)$$

for both the microgravity experiment

$$D'_{T,1}(\mathrm{THN}) = 0.988 \cdot 10^{-12}\,\mathrm{m}^2/(\mathrm{s}\cdot\mathrm{K}),$$
$$D'_{T,2}(\mathrm{IBB}) = -0.680 \cdot 10^{-12}\,\mathrm{m}^2/(\mathrm{s}\cdot\mathrm{K}),$$
$$D'_{T,3}(n\mathrm{C}_{12}) = -0.308 \cdot 10^{-12}\,\mathrm{m}^2/(\mathrm{s}\cdot\mathrm{K}),$$

and for the ground experiment

$$D'_{T,1}(\mathrm{THN}) = 0.690 \cdot 10^{-12}\,\mathrm{m}^2/(\mathrm{s}\cdot\mathrm{K}),$$
$$D'_{T,2}(\mathrm{IBB}) = -0.215 \cdot 10^{-12}\,\mathrm{m}^2/(\mathrm{s}\cdot\mathrm{K}),$$
$$D'_{T,3}(n\mathrm{C}_{12}) = -0.475 \cdot 10^{-12}\,\mathrm{m}^2/(\mathrm{s}\cdot\mathrm{K}).$$

5 Conclusions

We have determined the Soret (S_T) coefficients in the ternary mixture of 0.80/0.10/0.10 of THN-IBB-$n\mathrm{C}_{12}$ using raw data of run #18 of the DCMIX-1 microgravity experiment and using data obtained in a ground laboratory. The results exhibit reasonable quantitative agreement between the ground and microgravity experiments in the limits of the error bar.

$$S'^{\mathrm{Earth}}_{T,1}(\mathrm{THN}) = 1.035 \cdot 10^{-3}\,\mathrm{K}^{-1},$$
$$S'^{\mathrm{Earth}}_{T,2}(\mathrm{IBB}) = -0.093 \cdot 10^{-3}\,\mathrm{K}^{-1},$$
$$S'^{\mathrm{Earth}}_{T,3}(n\mathrm{C}_{12}) = -0.942 \cdot 10^{-3}\,\mathrm{K}^{-1},$$
$$S'^{\mathrm{ISS}}_{T,1}(\mathrm{THN}) = 1.426 \cdot 10^{-3}\,\mathrm{K}^{-1},$$
$$S'^{\mathrm{ISS}}_{T,2}(\mathrm{IBB}) = -0.767 \cdot 10^{-3}\,\mathrm{K}^{-1},$$
$$S'^{\mathrm{ISS}}_{T,3}(n\mathrm{C}_{12}) = -0.659 \cdot 10^{-3}\,\mathrm{K}^{-1}.$$

Besides the measured magnitude of the Soret coefficients we have proposed a way of estimating errors of the measurement and have discussed a specific feature of the errors. The diffusion (D) coefficients were measured on the ground using the Taylor Dispersion Technique, and the thermodiffusion (D_T) coefficients were calculated for the ground and microgravity experiments.

All the steps required to extract the transport coefficients from the raw data obtained in the SODI on board the ISS, as well as from the laboratory set-up, are discussed in detail.

In addition to the standard procedure, which includes extraction of the wrapped phase, phase unwrapping, subtraction of the reference phase image and transformation

of the phase map into the refractive index, some additional issues specific to the thermodiffusion experiment are discussed.

These issues consist of examining the neglected separation at the initial time interval (before the reference image), the under-evaluated separation due to spatial nonlinearity of the temperature field, and the mass exchange between working liquid volume and expansion volume. Two last corrections are specific to the microgravity cell design and are recommended to be used in the analysis of any DCMIX experiment because they allow approximately 10% of the component separation to be retrieved, which would otherwise be lost.

A thorough analysis of the results of the six-parameter fit indicated that it is not possible to extract the diffusion matrix and the thermal diffusion coefficients with a desirable accuracy from data obtained using the ODI technique. However, we have demonstrated the efficiency of the two-parameter fit for accurate reconstruction of the variation of the refractive index, from which concentration separations are obtained by solving a system of linear equations. The validity of this approach was confirmed by the fact that both eigenvalues obtained during the course of the diffusion experiment (Taylor Dispersion Technique) are similar for the considered mixture.

The authors would like to acknowledge the PRODEX programme of the Belgian Federal Science Policy Office. This work has been developed in the framework of the cooperative project DCMIX (AO-2009-0858/1056) of the European Space Agency and the Russian Space Agency (Roscosmos). The authors would also like to acknowledge an anonymous referee whose favourable but rigorous critics resulted in substantial improvement of the text.

References

1. A. Leahy-Dios, M.M. Bou-Ali, J.K. Platten, A. Firoozabadi, J. Chem. Phys. **122**, 234502 (2005).
2. A. Königer, H. Wunderlich, W. Köhler, J. Chem. Phys. **132**, 174506 (2010).
3. P. Blanco, M.M. Bou-Ali, J.K. Platten, D. Alonso de Mezquía, J.A. Madariaga, C. Santamaría, J. Chem. Phys. **132**, 114506 (2010).
4. A. Mialdun, V. Shevtsova, J. Chem. Phys. **138**, 161102 (2013).
5. M. Larrañaga, D.A.S. Rees, M.M. Bou-Ali, J. Chem. Phys. **140**, 054201 (2014).
6. V. Shevtsova, C. Santos, V. Sechenyh, J.C. Legros, A. Mialdun, Micrograv. Sci. Technol. **25**, 275 (2014).
7. A. Mialdun, C. Minetti, Y. Gaponenko, V. Shevtsova, F. Dubois, Micrograv. Sci. Technol. **25**, 23 (2013).
8. P. Hariharan, B.F. Oreb, T. Eiju, Appl. Opt. **26**, 2504 (1987).
9. V. Shevtsova, T. Lyubimova, Z. Saghir, D. Melnikov, Y. Gaponenko, V. Sechenyh, J.C. Legros, A. Mialdun, J. Phys.: Conf. Ser. **327**, 012031 (2011).
10. S. Mazzoni, V. Shevtsova, A. Mialdun, D. Melnikov, Yu. Gaponenko, T. Lyubimova, M.Z. Saghir, Europhys. News **41**, 14 (2010).
11. V. Shevtsova, A. Mialdun, D. Melnikov, I. Ryzhkov, Y. Gaponenko, Z. Saghir, T. Lyubimova, J.C. Legros, C.R. Méc. **339**, 310 (2011).
12. A. Mialdun, V. Shevtsova, J. Chem. Phys. **134**, 044524 (2011).
13. A. Mialdun, V. Sechenyh, J.C. Legros, J. Ortiz de Zárate, V. Shevtsova, J. Chem. Phys. **139**, 104903 (2013).
14. T. Kreis, *Handbook of Holographic Interferometry: Optical and Digital Methods* (Wiley, 2005).
15. A. Mialdun, V. Shevtsova, C.R. Méc. **339**, 362 (2011).
16. A. Mialdun, V. Yasnou, V. Shevtsova, A. Königer, W. Köhler, D. Alonso de Mezquia, M.M. Bou-Ali, J. Chem. Phys. **136**, 244512 (2012).
17. M. Gebhardt, W. Köhler, A. Mialdun, V. Yasnou, V. Shevtsova, J. Chem. Phys. **138**, 114503 (2013).
18. A. Königer, B. Meier, W. Köhler, Philos. Mag. **89**, 907 (2009).
19. J.F. Torres, A. Komiya, E. Shoji, J. Okajima, S. Maruyama, Optics Lasers Engin. **50**, 1287 (2012).
20. V. Sechenyh, J.C. Legros, V. Shevtsova, J. Chem. Thermodyn. **62**, 64 (2013).
21. R. Taylor, R. Krishna, *Multicomponent Mass Transfer*, Wiley Series in Chemical Engineering (Wiley, 1993).
22. A.C. Kak, M. Slaney, *Principles of Computerized Tomographic Imaging* (IEEE Press, 1988).
23. G.B. Ray, D.G. Leaist, J. Chem. Eng. Data **55**, 1814 (2010).